ASME Journal of Engineering for Gas Turbines and Power
Online journal at:
https://asmedigitalcollection.asme.org/gasturbinespower

R. Gioia
Department of Energy,
Politecnico di Milano,
Milano 20156, Italy

S. Ottaviano
Department of Industrial Engineering,
University of Bologna,
Bologna 40136, Italy

A. Romei
Department of Energy,
Politecnico di Milano,
Milano 20156, Italy

A. Peretto
Department of Industrial Engineering,
University of Bologna,
Bologna 40136, Italy

L. Branchini
Department of Industrial Engineering,
University of Bologna,
Bologna 40136, Italy

A. Spinelli[1]
Department of Energy,
Politecnico di Milano,
Milano 20156, Italy
e-mail: andrea.spinelli@polimi.it

Optimal Cycle and Turbine Design For MW-Scale Waste Heat Recovery Organic Rankine Cycle With Partial Evaporation

Efficiently converting waste heat into electricity is crucial for enhancing energy sustainability. Partial evaporation organic Rankine cycle (PE-ORC) technology with wet-to-dry expansion has demonstrated improved conversion efficiency by optimizing heat source utilization over conventional subcritical organic Rankine cycles (ORCs). However, PE-ORCs face challenges at the MW scale, such as defining optimal operating conditions and designing turbo-expanders for two-phase mixtures. This paper presents a model to determine optimal PE-ORC conditions for specific waste heat sources and outlines a methodology to design a single-stage turbine operating with wet-to-dry expansion and a dry-operated rotor. Two cycle optimizations, for high and low-temperature ranges of the heat source and based on real data, show that PE-ORC is competitive for the low-temperature range, with an increase of power production of about 25% compared to the best single-phase cycle. A radial inflow turbine design for the low-temperature cycle is presented, focusing on the design, through shape optimization, of the stator cascade, the most critical component due to the supersonic and two-phase flow. The optimum profile is then simulated together with a nonoptimized rotor via Computational Fluid Dynamic tool, confirming the possibility of designing a two-phase turbine with an efficiency higher than 85%, as assumed during the cycle design. [DOI: 10.1115/1.4069578]

Keywords: organic Rankine cycle, partial evaporation, cycle and turbine optimization, wet-to-dry expansion, radial inflow turbine optimization

1 Introduction

Industrial processes are responsible for a significant amount of energy loss as waste heat. Recent estimates pointed out that more than 50% of worldwide energy consumption is released as streams of fluids (water, flue gases, etc.) at diverse temperature levels, from which waste heat can be recovered. The EU (European Union) waste heat recovery (WHR) potential from industry amounts to 920 TWh/year (10% of which for Italy), mostly available at temperatures below 400 °C [1]. Decisive sectors are energy-intensive industries, especially iron, steel, chemical, paper, food, glass, and cement. Regarding the ceramic tiles industry, a facility with an average tile production of 10 tons/h discharges about 3.3 MW of waste heat, of which more than 80% is at temperatures between 100 and 250 °C. In the glass industry, the primary source of waste heat is represented by the hot gases from the melting furnaces, which are available at temperatures between 400 and 500 °C. The iron and steel industry offers several sources of waste heat at different conditions, such as the electric arc furnace (high temperature and flowrate of exhaust gas), the submerged arc furnace, or the sinter cooler (medium temperature and high flowrate). For example, an electric arc furnace with a capacity of 100 tons/h of steel scrap would provide high-quality waste heat for more than 13 MW. In this case, the heat carrier is often condensing steam.

The most effective way to utilize the recovered energy is through electricity generation. Considering temperature levels and sizes of installation (up to 50 MW), the Organic Rankine Cycle (ORC) is the most viable technology for industrial WHR conversion into electricity. From this perspective, the untapped energy potential is prudently estimated as 5% of the overall electricity demand, corresponding to 150 TWh/year for the EU and 15 TWh/year for Italy [2]. ORC is a well-established technology for the conversion of thermal power at low-medium temperatures (below 400 °C) [3], with the subcritical configuration as the only deployed arrangement at a commercial scale (TRL 9). Despite its advantages, the ORC faces challenges, including high investment costs and relatively low power production efficiency, primarily due to irreversibility in the

---

Turbo Expo: Turbomachinery Technical Conference & Exposition (GT2025), June 16–20, 2025. GT2025.

[1] Corresponding author.

Manuscript received July 15, 2025; final manuscript received July 28, 2025; published online October 25, 2025. Editor: Jerzy T. Sawicki.

heat exchange process. These challenges complicate the sizing of critical components (heat exchanger, expander, and pump) and the selection of optimal working fluids. Proper fluid selection is crucial for matching the temperature profile of the waste heat source, thereby enhancing system performance.

To overcome these challenges, advanced methods are being explored, such as using dry fluids that facilitate a wet-to-dry transition during expansion. The working principle of an ORC system operating with a two-phase expansion is identical to a standard ORC, but the working fluid at the expander inlet is a mixture of liquid and vapor, rather than superheated/saturated vapor. Accordingly, in wet-to-dry cycles, the heat exchange does not involve complete vaporization, possibly leading to lower irreversibility and improved efficiency [4]. Figure 1 highlights ORC cycles in which the expansion process occurs under two-phase conditions, just initially, due to the retrograde saturation curve. This approach offers the benefit of reduced exergy loss through the evaporator, as the heat exchange process concludes near the pinch point, minimizing irreversibility [5]. Fischer [6] estimated a 14–29% increase in exergy efficiency for partial evaporation organic Rankine cycle (PE-ORCs) compared to traditional subcritical ORCs.

According to the typical power size of WHR applications in the industrial sector (MW scale) and the temperature level at which most of the recoverable heat is available, turbo-expanders are the more efficient solution for power extraction. However, when partial evaporation is introduced, the turbine becomes a critical component due to the additional losses due to two-phase interaction and possible rotor blade erosion from impinging droplets. Appropriate tools are required to design PE-ORC turbo-expanders and to evaluate their performance, which are currently lacking.

Researchers have focused on positive-displacement expanders, such as piston and twin-screw designs, which can handle multiphase mixtures [7–9]. However, these expanders are typically efficient only for small systems (kW scale), and their built-in volume ratios can limit achievable expansion ratios [10], restricting their applicability to low-temperature scenarios (up to 150 °C). For higher heat-source temperatures and MW-scale applications, turbo-expanders may be necessary, but existing turbine designs struggle with efficiently handling two-phase mixtures, leading to additional losses. Recent advancements in the thermodynamics of molecularly complex organic fluids suggest that flashing processes can lead to complete vaporization into superheated vapor [11]. This concept, initially introduced by Elliott [12] and recently revisited by White [13], proposes turbomachinery with estimated efficiencies exceeding 85%, where nozzle vanes expand two-phase flows and deliver superheated vapor to rotating blade rows. White [14] emphasized the importance of nonequilibrium effects for achieving full vaporization through nozzle cascades, indicating that experimental validation is necessary. The dataset by Zhu and Elbel [15] is currently the only literature source on experiments with flashing flows of organic compounds. However, the refrigerant R134a used in their studies lacked the molecular complexity to observe wet-to-dry expansions and was tested under conditions not relevant to PE-ORCs. Zhu and Elbel [16] found good agreement between standard computational fluid dynamics (CFD) methods and experimental data regarding pressure distribution and mass flowrate, although phase stratification was noted in numerical flow fields that did not appear in optical visualization. Tammone [17] highlighted that equilibrium-based numerical methods could lead to significant errors (up to 50%) in mass-flowrate and pressure distribution estimates.

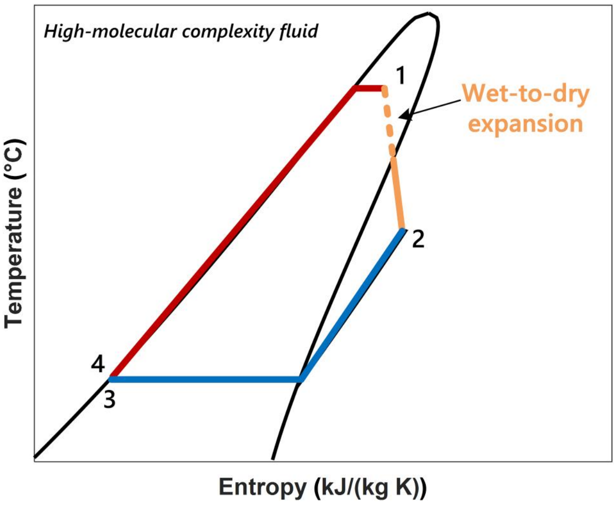

Fig. 1 Representative T-s diagram with wet-to-dry expansion of high molecular complexity fluid

Given the need to improve the efficiency of waste-heat recovery systems and promote broader adoption of PE-ORC technologies, this paper presents a methodology developed to investigate the design of an MW-scale PE-ORC system operating with organic fluids that allow a wet-to-dry expansion across the turbine. The outcomes of this study include:

- the development of a calculation model aimed at identifying optimal system architecture, optimal working fluid, and operating conditions of a PE-ORC cycle to maximize power output depending on the heat source characteristics (i.e., relevant industrial cases of waste heat sources, in the low/medium-temperature range);
- the aerodynamic design of a radial inflow single-stage turbine implementing wet-to-dry expansion.

2 Cycle Optimization

The first part of the study is focused on determining the optimum working fluid and operating conditions to maximize power output, assessed within two case studies related to real-world examples of waste heat recovery applications using ORCs. Selected cases are representative of two temperature levels, namely, high and low temperature. The optimization routine is divided into two consecutive steps:

- fluid prescreening, aimed at identifying a list of working fluids to be analyzed in the ORC modeling and optimization task;
- optimization of operating conditions, for each prescreened fluid. This task includes a genetic algorithm and a simplified thermodynamic model of the ORC.

The purpose of this analysis is to establish optimal cycle conditions to inform the design of the radial turbine in the second part of the study.

2.1 Fluid Prescreening.

The fluid prescreening is designed to identify a list of substances to be considered in the modeling and optimization task. The screening is carried out by considering all the pure fluids included in the open-source library CoolProp [18], constrained by four criteria specified below.

2.1.1 Environmental Impact. Fluids must exhibit zero ozone depletion potential (ODP) and low global warming potential ($GWP < 750$).

2.1.2 Saturated Vapor Curve. This criterion restricts the selection to dry and isentropic fluids, by using the definition of molecular complexity, σ [14], in Eq. (1). The σ value is calculated at a reference temperature set to 80% of the critical temperature to ensure that the analysis appropriately accounts for substances exhibiting dry behavior within the evaporation temperature range relevant to their use in an ORC system. Fluids must exhibit positive values of σ to be included in the cycle optimization.

$$\sigma = \frac{ds}{dT} \, @ \, 0.8 \, T_{\text{crit}}(\text{K}) \tag{1}$$

2.1.3 Minimum Acceptable Condensation Pressure. The employment of very low-pressure condensing fluids may be impractical due to air infiltration risks in low-pressure equipment. Hence, this criterion limits the choice to substances with condensation pressure higher than $P_{k,\text{min}} = 0.005\,\text{MPa}$ at a fixed condensation temperature of 30 °C.

2.1.4 Expected Thermal Performance. An initial assessment of the thermodynamic performance of each fluid is conducted using an adapted Jacob number (Ja) [19]. The value of Ja is calculated according to Eq. (2) within fixed values of evaporation temperature and condensation pressure, for each of the fluids that have passed through previous screening criteria.

$$\text{Ja} = \frac{h_v(T_{\text{vap}}) - h_{\text{is}}(P_k)}{h_v(T_{\text{vap}}) - h_l(T_{\text{vap}})} \tag{2}$$

Subscripts v and l in Eq. (2) refer to saturated vapor and saturated liquid, respectively, both calculated at the vaporization temperature T_{vap}, while symbol $h_{\text{is}}(P_k)$ represents the outlet enthalpy of the ideal (isentropic) transformation, calculated via CoolProp at the condensation pressure (P_k). The value of vaporization temperature T_{vap} in Eq. (2) is selected based on the fluid critical temperature and heat source inlet temperature, according to the criterion expressed in the following equation:

$$T_{\text{vap}} = \begin{cases} 0.9 \cdot T_{\text{cr}} \text{ if } T_{H,\text{in}} > 0.9 \cdot T_{\text{cr}} \\ T_{H,\text{in}} \text{ if } T_{H,\text{in}} < 0.9 \cdot T_{\text{cr}} \end{cases} \tag{3}$$

In this form, the Jacob number designates the weight of the ideal expansion work compared to the latent heat of vaporization. A high value of the Jacob number indicates that a smaller portion of the heat transfer process in the evaporator is attributed to latent heat, which can enhance the efficiency of heat exchangers and overall cycle performance [20]. The Jacob number is first calculated for all the fluids under consideration. Then, the fluid with the highest Jacob number (Ja_{max}) is identified. Finally, any fluid whose Jacob number is at least half of the maximum Jacob number is deemed acceptable based on the criterion ($\text{Ja} > 0.5 \cdot \text{Ja}_{\text{max}}$). This threshold ensures that only fluids with sufficiently high expansion work potential relative to latent heat effects are selected.

2.2 Cycle Modeling and Optimization. The ORC system under consideration is illustrated in the simplified layout in Fig. 2, consisting of three heat exchangers (evaporator, condenser, and recuperator), a feed pump, and a turbine. The modeling approach employs a lumped-parameter method to perform thermal balances across the key processes, which are:

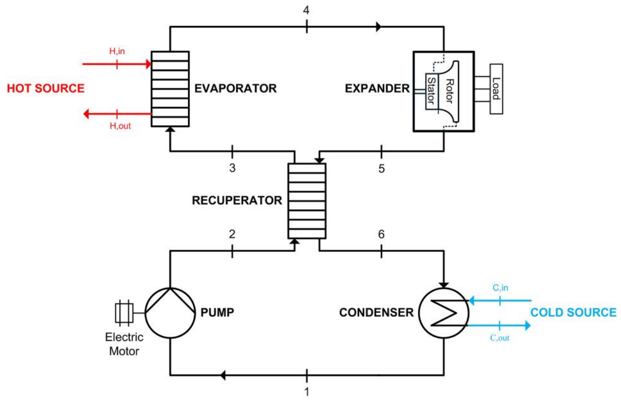

Fig. 2 Schematic layout of ORC system modeled

Table 1 Main equations used in the ORC model

Component	Equation
Evaporator	$\dot{Q}_{\text{ev}} = \dot{m}_H \cdot c_H(T_{H,\text{in}} - T_{H,\text{out}}) \cdot \eta_{\text{ev}} = \dot{m}_{\text{ORC}} \cdot (h_4 - h_3)$ (4)
	$\Delta T_{\text{sh}} = T_4 - T_{\text{vap}}$ (5)
	$\varepsilon_{\text{ev}} = \frac{T_{H,\text{in}} - T_{H,\text{out}}}{T_{H,\text{in}} - T_3}$ (6)
	$X_4 = \begin{cases} 1 + \frac{T_4 - T_{\text{vap}}}{T_{H,\text{in}} - T_{\text{vap}}} \; if\; X_4 > 1 \\ \frac{m_v}{m_l + m_v} \; if\; X_4 < 1 \end{cases}$ (7)
	$\Delta T_{\text{pp,ev}} = T_{H,\text{pp}} - T_{\text{vap}}$ (8)
Turbine	$\eta_{\text{turb}} = \frac{h_4 - h_5}{h_4 - h_{5,\text{is}}}$ (9)
	$\dot{W}_{\text{turb}} = \dot{m}_{\text{ORC}} \cdot (h_4 - h_5) \cdot \eta_{\text{em}}$ (10)
Recuperator	$\dot{Q}_{\text{rec}} = \dot{m}_{\text{ORC}} \cdot (h_3 - h_2) = \dot{m}_{\text{ORC}} \cdot (h_5 - h_6)$ (11)
	$\varepsilon_{\text{rec}} = \frac{h_5 - h_6}{\Delta h_{\text{max}}}$ (12)
Feed-pump	$\eta_p = \frac{P_2 - P_1}{\rho \cdot (h_2 - h_1)}$ (13)
	$\dot{W}_p = \dot{m}_{\text{ORC}} \cdot (h_2 - h_1)/\eta_{\text{em}}$ (14)
Condenser	$\dot{Q}_k = \dot{m}_C \cdot c_C(T_{C,\text{out}} - T_{C,\text{in}}) = \dot{m}_{\text{ORC}} \cdot (h_6 - h_1)$ (15)
	$\Delta T_{\text{pp},k} = T_k - T_{C,\text{pp}}$ (16)
	$\Delta T_{\text{sc}} = T_k - T_1$ (17)
ORC performance	$\dot{W}_{\text{net}} = \dot{W}_{\text{turb}} - \dot{W}_p$ (18)
	$\eta_{\text{ORC}} = \frac{\dot{W}_{\text{net}}}{\dot{Q}_{\text{ev}}}$ (19)

- Pumping process in the feed pump (1–2).
- High-pressure liquid pre-heating in the recuperator (2–3).
- Heating and vaporization of high-pressure liquid in the evaporator (3–4).

- Expansion of high-pressure vapor in the turbine (4–5).
- Cooling of low-pressure vapor in the recuperator (5–6).
- Condensation of low-pressure vapor in the condenser (6–1).

During the optimization, both ORC configurations with simple and recuperated cycles are modeled. In the case of a simple cycle, points 2 and 3 coincide, as points 5 and 6.

The model inputs are the design conditions of the heat source at the evaporator inlet, which include the heat transfer medium (oil or water), the temperature ($T_{H,\mathrm{in}}$), and the flowrate ($\dot{m}_H$), and the temperature of the cooling water at the condenser inlet ($T_{C,\mathrm{in}}$).

The list of equations implemented in the ORC model is reported in Table 1, with reference to the generic T-s diagram of Fig. 3 and to the Nomenclature section for symbols.

The following assumptions are considered in the ORC model:

- the cycle is modeled in steady-state conditions;
- pressure losses are assumed constant, with a total value $\Delta P_{\mathrm{tot}} = 10\%$ distributed between the evaporator, condenser, and recuperator [3];
- in the evaporator and condenser, the minimum temperature difference between the fluids (ΔT_{pp}), which can occur at the inlet, outlet, or at the saturation line, is assumed equal to 7 K;
- thermal losses in the evaporator are taken into account, assuming an insulation efficiency equal (η_{ev}) to 0.98;
- the electro-mechanical efficiency (η_{em}) is assumed equal to 0.9 for both the pump and the turbine.

System optimization is performed using the Non-Dominated Sorting Genetic Algorithm implemented in the open-source Python library Pymoo [21]. The problem is formulated with a single-objective optimization function maximizing the net power output of the ORC system, defined in Eq. (18). The population size and number of generations were set at 60 and 20, respectively. The value choice ensures sufficient exploration of the design space while maintaining manageable computational costs. Additionally, Latin Hypercube Sampling has been used to generate a well-distributed initial population, reducing the likelihood of premature convergence to local optima. The crossover distribution index is set to 10 with a probability of 0.9, while the mutation index is set to 20 with a probability of 0.3, ensuring a balance between exploration and exploitation.

The definition and range of variation of the optimization variables are presented in Table 2, which also reports the values of the fixed parameters utilized in the model.

The optimization variables selected are the reduced evaporation pressure (P_r), the turbine inlet state parameter (X_4), the evaporator effectiveness ($\varepsilon_{\mathrm{ev}}$), and the recuperator effectiveness ($\varepsilon_{\mathrm{rec}}$). The meaning of the parameter X_4 changes depending on the value it assumes during the optimization process. In particular, when X_4 is greater than 1, it implies that the cycle is superheated (see Fig. 3(*a*)), with the value of X_4 correlating to the superheating degree at the turbine inlet, as illustrated by Eq. (7). Conversely, when X_4 is between 0 and 1, it denotes a partial evaporation condition (see Fig. 3(*b*)), with the value of X_4 corresponding to the vapor quality at the turbine inlet. In the presence of a wet-to-dry expansion ($X_4 < 1$) an additional constraint is applied to include only cases in which the ratio of the dry expansion enthalpy drop to the total enthalpy drop (in isentropic conditions) is greater than 10%. Furthermore, in case the algorithm converges to $\varepsilon_{\mathrm{rec}} < 0.1$, the cycle is modeled without the recuperator to eliminate the associated pressure drop.

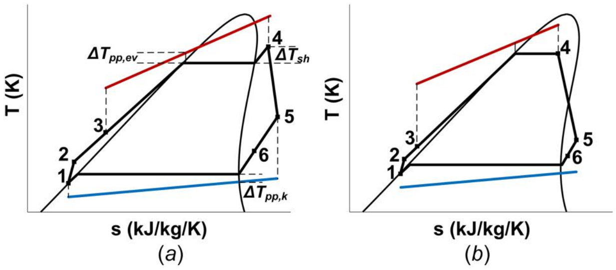

Fig. 3 T-s diagram of ORC system with dry expansion (*a*) and wet-to-dry expansion (*b*)

2.3 Case Studies. The cycle optimization is applied to two case studies, characterized by different temperature levels of the heat source. They have been selected from existing industrial applications for which information about the waste heat source was available. Selected examples are significant in the waste heat recovery field, as are referred to cement and ceramic industries, which are significant industrial sectors providing a relevant amount of medium to high-quality waste heat.

CASE STUDY 1—High Temperature (HT)

The first case study refers to waste heat recovery from a large-scale cement factory in northern Italy, characterized by a production capacity of 2500 tons of clinker per day. An ORC unit with a nominal capacity of 3.5 MW, supplied by the company Exergy, has been in operation at this factory since 2020 [22]. The evaporator of the ORC unit is fed with a flow of diathermic oil, which is heated to a temperature of 280 °C by the gas stream from the kiln preheater and the clinker cooler. The nominal oil mass flowrate is equal to 38.4 kg/s.

CASE STUDY 2—Low Temperature (LT)

The second case study concerns a ceramic tile factory in Italy with a nominal capacity of 144,000 tons of tiles per year. The plant releases waste heat through the flue gas and cooling air of four kilns, which are mixed to form a stream with a total flowrate of 140,000 Nm^3/h and an average temperature of 250 °C. No waste heat recovery system is currently installed. The design of the ORC system envisages the installation of an intermediate loop fed with pressurized water at 1 MPa, entering the ORC evaporator with a temperature of 165 °C and a mass flowrate equal to 13.8 kg/s.

2.4 Cycle Optimization Results. The fluid prescreening has resulted in the list of fluids shown in Table 3 for the HT case and Table 4 for the LT case. Within the HT case, a list of 10 fluids is obtained from the prescreening, including alkanes (cyclopentane, cyclohexane, n-hexane, n-heptane, isohexane), aromatic hydrocarbons (benzene, toluene), siloxane (MM), carbonate ester (dimethyl carbonate) and chlorinated hydrocarbon (dichloroethane). The tables also show the main operating variables corresponding to the optimum conditions obtained with each fluid. The presence or absence of the recuperator is indicated in the last column of the table (REC). Focusing on the HT case, the net power output obtained for the optimum operating conditions is shown in Fig. 4.

The power output ranges between 3.0 MW and 4.1 MW, with the global maximum achieved using cyclopentane in a slightly superheated cycle ($X_4 = 1.03$) without recuperator, with an overall efficiency of 22%, in line with efficiency values reported for similar commercial applications [23,24]. This condition is also characterized by a relatively low value of the expansion ratio (β), equal to 62, and a condensation pressure slightly below ambient pressure (0.067 MPa). The thermodynamic cycle corresponding to the optimal condition is represented in the T-s diagram in Fig. 5.

A good performance is also obtained with a trilateral-close cycle ($X_4 = 0.04$) working with Cyclohexane, which achieves a net power of over 3.9 MW operating a wet-to-dry expansion, and an overall efficiency of 21%. However, in this case, the pressure ratio was approximately 167, which may necessitate a multistage turbine arrangement. The highest value of efficiency was 26%, obtained with MM as working fluid with dry expansion, which achieved a net power output slightly above 3.2 MW.

The list of fluids resulting from the prescreening within the LT case contains a total of 17 substances from different categories,

Table 2 Optimization variables and parameters

Variable	Definition	Range of variation
Reduced evaporation pressure, P_r	$P_r = \frac{P_{\text{vap}}}{P_{\text{crit}}}$	0.1–0.9
State parameter at the expander inlet, X_4	Eq. (7)	0–1.95
Evaporator effectiveness, ε_{ev}	Eq. (6)	0.1–0.9
Recuperator effectiveness, ε_{rec}	Eq. (12)	0–0.85
Parameter	Definition	Value
Turbine efficiency, η_{turb}	Eq. (9)	0.90 if $X_4 > 1$ 0.85 if $X_4 < 1$
Feed-pump efficiency, η_p	Eq. (13)	0.7
Subcooling at condenser outlet	Eq. (17)	7 K
Minimum pinch point temperature difference @ evaporator and condenser	Eqs. (8) and (16)	7 K

Table 3 Cycle optimization results for HT case

Fluid	X_4	$\dot{W}_{\text{net}}$ (kW)	$\dot{m}_{\text{ORC}}$ (kg/s)	P_{vap} (MPa)	P_k (MPa)	β	REC
Cyclopentane	1.03	4090	29.4	4.110	0.067	62	N
Cyclohexane	0.04	3923	30.0	3.652	0.022	167	N
n-Hexane	0.98	3654	28.2	2.737	0.033	83	Y
n-Heptane	0.15	3576	28.7	2.377	0.011	221	Y
Isohexane	0.99	3538	30.4	2.713	0.045	60	Y
Toluene	0.81	3345	31.1	0.563	0.007	82	Y
MM	0.99	3239	37.3	1.461	0.010	147	Y
Benzene	1.00	3234	24.8	1.177	0.022	55	N
DimethylCarb.	0.91	3224	29.3	0.908	0.013	69	Y
Dichloroethane	1.22	3030	29.5	0.880	0.018	48	N

including hydrocarbons, hydrofluorocarbons, siloxanes, and hydrofluoroolefins (see Table 4).

The optimization routine applied to this set of fluids yielded the performance results presented in Fig. 6. The power output exhibits a range of 0.5 MW–0.8 MW. The fluid with the highest performance was the Novec649, a nonflammable and ultralow GWP fluorinated ketone. This fluid was observed to achieve a net power output of approximately 780 kW with an efficiency of 14%, operating with a partially evaporated cycle with a recuperator. This cycle features a wet-to-dry expansion with a vapor quality at the expander inlet close to 0.4 and an expansion ratio of 17. The T-s diagram about this condition is presented in Fig. 7.

In this LT case, high values of total efficiency were also observed using the hydrocarbons cyclopentane and n-hexane (13% and 14% respectively), which however achieved substantially lower values of power output (around 550 kW), operating in both cases with a dry expansion ($X_4 \cong 1.0$). The efficiencies obtained from these simulations are consistent with the values reported in manufacturers' data for similar applications [25].

Due to the favorable performance and characteristics observed with Novec649, including its low environmental impact and safety issues, this fluid was selected for the two-phase turbine design, also considering the modest value of β which represents a favorable design condition, as it is suitable for a single-stage radial turbine.

3 Two-Phase Turbine Design

As reported in the introduction, the only off-the-shelf component of a MW-scale PE-ORC is the turbo-expander. For this reason, a detailed design of this component is presented, focusing on the main challenges associated with the machine two-phase nature.

In agreement with previous works [13,26], the selected turbine is a single-stage radial-inflow design, where the stator fully vaporizes the liquid by leveraging the retrograde saturation curve. The rotor

Table 4 Cycle optimization results for LT case

Fluid	X_4	$\dot{W}_{\text{net}}$ (kW)	$\dot{m}_{\text{ORC}}$ (kg/s)	P_{vap} (MPa)	P_k (MPa)	β	REC
Novec649	0.42	784	48.6	1.09	0.065	17	Y
Neopentane	0.77	641	14.3	1.71	0.247	7	N
MM	0.58	636	17.9	0.20	0.010	20	N
Iso-Butene	1.01	625	12.8	1.95	0.432	5	Y
n-Butane	0.99	623	12.8	1.58	0.348	5	N
1-Butene	1.01	622	12.0	2.08	0.421	5	N
trans-2-Butene	1.00	603	10.8	1.73	0.336	5	N
R245ca	1.03	602	21.0	0.93	0.156	6	Y
DiethylEther	0.98	601	11.6	0.66	0.111	6	N
R1234ze(Z)	1.10	601	21.5	1.33	0.264	5	Y
Isohexane	0.98	591	11.2	0.33	0.045	7	Y
n-Pentane	1.02	587	10.9	0.61	0.105	6	Y
cis-2-Butene	1.10	585	10.9	1.38	0.309	4	Y
Isopentane	1.01	581	10.5	0.86	0.138	6	N
SES36	0.98	567	27.4	0.64	0.106	6	Y
Cyclopentane	1.00	559	9.0	0.46	0.067	7	N
n-Hexane	0.98	551	8.4	0.36	0.033	11	Y

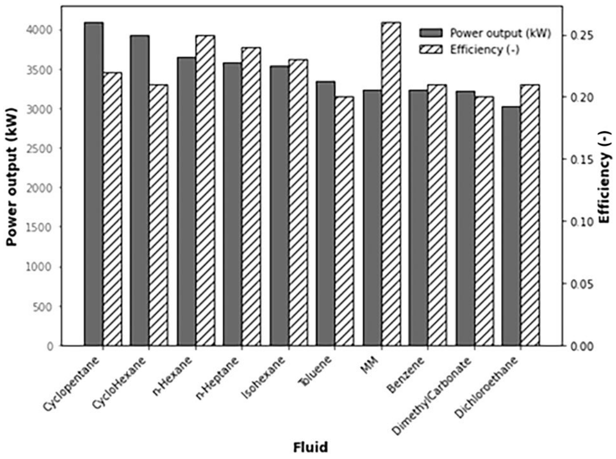

Fig. 4 Net power output and efficiency of most performing fluid for HT case

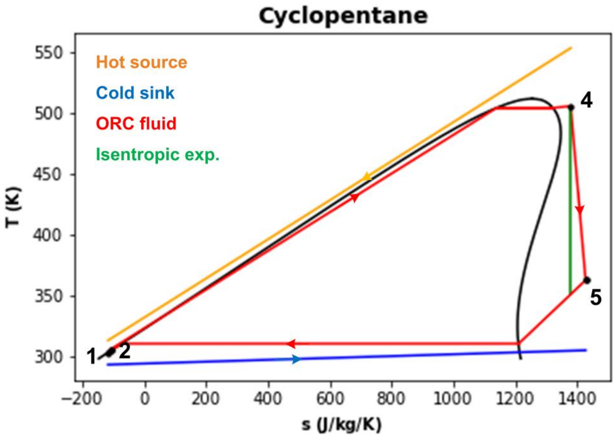

Fig. 5 Optimum T-s diagram of cyclopentane for HT case (simple cycle). Points 2–3 and 5–6 coincide.

then expands the superheated vapor, as a conventional centripetal rotor, without experiencing additional mechanical issues or aerodynamic losses associated with two-phase flows in the rotating cascade.

A mean-line code is first employed to define the turbine main geometry, followed by a detailed design of the stator, which is the most critical component. Finally, the complete turbine is simulated using CFD, with a focus on the comparison of the efficiency computed by either the mean-line method or the CFD.

3.1 Turbine Mean-Line Design.

An in-house mean-line code, already validated for single-phase radial inflow ORC turbines [27], is employed to define the preliminary turbine design. This code solves the one-dimensional continuity, momentum, and energy equations, with additional correlations to compute both losses and flow deviations. The main turbine components, modeled by the code, are (i) the vaned stator, (ii) the vaneless stator, (iii) the rotor, and (iv) the diffuser. While the relative flow in the rotor and the absolute flow in the diffuser are both subsonic, supersonic flow is expected in the stator due to the high expansion ratio and the very low speed of sound characteristic of an organic two-phase flow [13]. The stator vanes are therefore designed with a convergent-divergent geometry.

It is noteworthy that the loss correlation for the rotor, where the vapor is superheated, has been validated by Manfredi et al. [27], whereas the lack of experimental data on two-phase expansions has prevented the validation of the loss correlations applied to the stator. A loss breakdown of a two-phase turbine computed using the employed code was performed by Romei et al. [26], showing that doubling the nozzle passage losses [28], to mimic the enhanced friction due to the interaction between the two phases [29], the turbine efficiency remains above 85%. Regarding the diffuser, the primary loss source in the employed model, developed by Agromayor et al. [30], is the friction between the diffuser wall and the flow. This contribution is evaluated by assuming a skin friction coefficient of 0.029, which best approximates the experimental results used to validate the method [30].

The two-phase expansion in the stator is modeled employing a homogeneous equilibrium model, which assumes no slip between the two phases and thermodynamic equilibrium, promoted by the already wet mixture at the turbine inlet [31]. The thermodynamic library CoolProp [32] was used in the mean-line code, with the NIST REFPROP backend [33] providing quantities unavailable from the former.

The turbine geometry was obtained through an optimization process that maximizes total-to-static efficiency. The total inlet conditions, mass flowrate, and static outlet pressure are set equal to the values computed via the cycle optimization in Sec. 2.4. The constraints and design variables are the same as in Ref. [26], encompassing manufacturing, geometrical, and aerodynamic considerations. Due to the two-phase flow at the inlet, a constraint on the maximum stator outlet pressure is imposed to ensure complete vaporization at the stator outlet. The optimization routine includes an initial global optimization with a differential evolution algorithm,

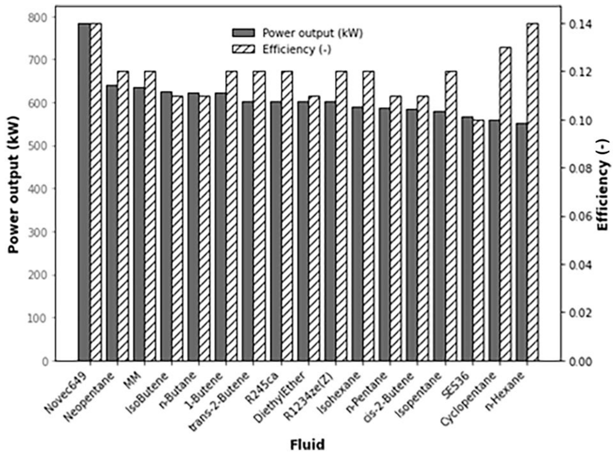

Fig. 6 Net power output and efficiency of most performing fluid for LT case

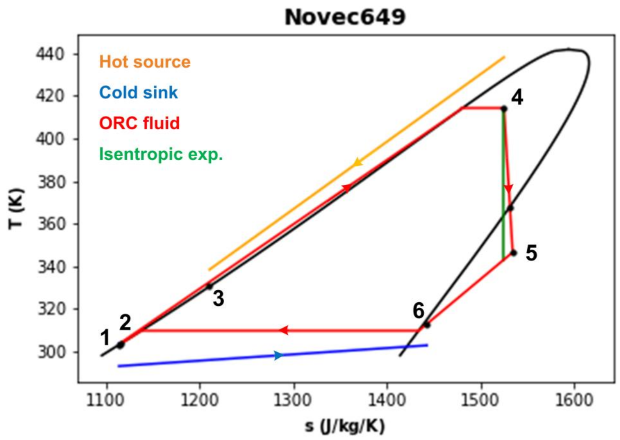

Fig. 7 Optimum T-s diagram of Novec649 for LT case (recuperated cycle)

followed by a local optimization based on least-squares quadratic programming, which is capable of handling nonlinear constraints.

Considering the two case studies in Sec. 2, only the turbine for the best cycle (a PE-ORC) of the LT case is designed. A turbine for the HT case is not considered since the power output of the best two-phase cycle (4% lower than the best single-phase cycle) does not justify the inherently higher complexity of a two-phase turbine design. This complexity is further amplified by the very large values of $\beta_{TS} = 167$ and $VR = 697$, which would necessarily require a multistage arrangement. However, such an arrangement is hindered by the necessity of confining the two-phase expansion within the stator.

3.1.1 Low Temperature Mean-Line Design. As reported in Sec. 2.4, the best two-phase cycle produces 25% more power than the best single-phase cycle, justifying the choice of addressing the higher complexity of the two-phase turbine design. Challenges are reduced compared to the best two-phase cycle for the HT case, due to the lower β_{TS} of 17 and VR of 45.

The optimal turbine design exhibits a relatively low rotational speed, equal to 3700 rpm, and, consequently, a relatively large inlet diameter, equal to 0.818 m. The specific speed is equal to 0.09, a value similar to that of optimized single-phase radial-inflow turbines [34].

The computed rotational speed is relatively close to 3000 rpm. Therefore, to allow for direct coupling with a 50 Hz operating grid, an additional optimization with a fixed rotational speed of 3000 rpm was carried out. Although a small reduction (about 1%) in efficiency is observed in the newly designed turbine, the lower cost and complexity of the system justify this choice.

Thus, the final turbine design exhibits a 3000 rpm rotational speed, an outlet stator angle of 78 deg, and a fully subsonic rotor (relative frame), facilitating both design and operation. The meridional representation of the optimal turbine is reported in Fig. 8.

The requirement to ensure single-phase vapor at the stator outlet results in a stage with a degree of reaction of 0.31, guaranteeing a pressure near half of the saturation pressure at the stator outlet, thereby ensuring that only vapor enters the rotor. Even if the actual recoverable kinetic energy is limited due to the large rotor outlet area ($r_{\mathrm{rot,out},h}/r_{\mathrm{rot,out},sh} = 0.4$), the diffuser increases the machine efficiency by about 0.6%. The limited pressure recovery is also related to the low diffuser area ratio, equal to 1.4, settled to limit the diffuser length. Even with this small area ratio, the low opening angle, selected to avoid flow separation, entails a diffuser length equal to three and a half times the rotor axial length, as shown in Fig. 8.

Since the complexity of the turbine design is primarily associated with the stator, a detailed design of this component was performed and is discussed in Sec. 3.2.

3.2 Stator Design. The two-phase nature of the flow prevents the use of the typical strategy applied to design a converging-diverging stator in single-phase applications. This strategy consists of two main steps: (i) designing the divergent portion using the Method of Characteristics (MoC) and (ii) constructing the blade through a series of geometrical transformations. However, when a two-phase expansion occurs in the divergent part, the MoC cannot be employed, as illustrated below.

The MoC is a marching-type analytical method used to design the supersonic portion of a nozzle under the assumptions of steady, two-dimensional, planar or axisymmetric, irrotational, and supersonic flow. It works by solving a hyperbolic system of partial differential equations [35]. Typically, the MoC is valid only if the Mach number remains continuous and monotonic, two conditions that may not hold in two-phase flows [19]. While nonmonotonicity can be addressed by modifying the marching method through various strategies [35], no established solution has been identified to handle the Mach discontinuity that may arise at the onset and completion of vaporization. Additionally, the lack of an accurate model to initialize the method raises questions about its reliability. Since the MoC requires $M > 1$, an accurate approach for assigning the initial conditions is essential. Although different initialization methods exist for both ideal [35] and nonideal [36] vapor flows, no equivalent approach is currently available for two-phase flows. Given that the accuracy of the MoC heavily depends on the initialization method, this limitation makes it unsuitable for designing efficient two-phase nozzles.

To address this issue, the following methodology is employed. First, a converging-diverging stator is designed using the conventional MoC for an expansion process occurring at the same inlet and outlet pressure in the superheated vapor region (single-phase). The resulting profile is then refined through a shape optimization routine aimed at minimizing losses.

3.2.1 Kriging Surrogate Model. Due to the different thermodynamic conditions at the stator inlet, the actual flow at the outlet of the blade designed using the MoC is not adapted, leading to an increase in fish-tail shock intensity and the possible formation of shocks within the blade passage [37]. This phenomenon-negatively impacts overall turbine efficiency. To mitigate this issue, the base profile is redesigned through shape optimization using a Kriging surrogate model.

Shape optimization involves evaluating multiple geometries to identify the one that minimizes a given objective function. However, performing this evaluation via CFD, as is common in turbomachinery design, incurs a prohibitive computational cost. The Kriging surrogate model addresses this challenge by constructing a metamodel through Gaussian regression [38], significantly reducing the number of required simulations. Initially, the model is trained on a set of simulated geometries, after which it is used to search for the global optimum. The risk of converging to a local rather than a global optimum is mitigated by iteratively adding new points to the training set using an infill criterion. Specifically, the expected improvement (EI) method was employed in this study [39].

Notably, EI leverages the Kriging model ability to predict both the mean value and the uncertainty of the objective function. This

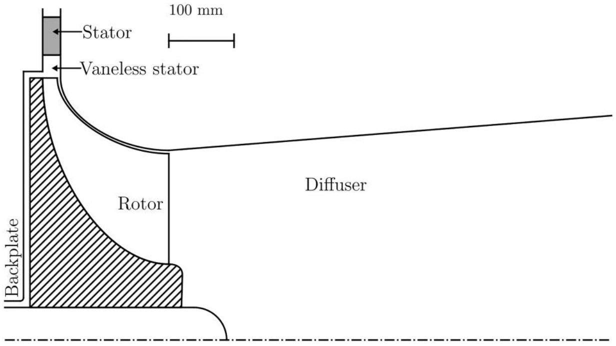

Fig. 8 Radial-inflow turbine sketch with main components modeled by mean-line code; represented dimensions are the ones of LT case turbine with rotational speed fixed at 3000 rpm

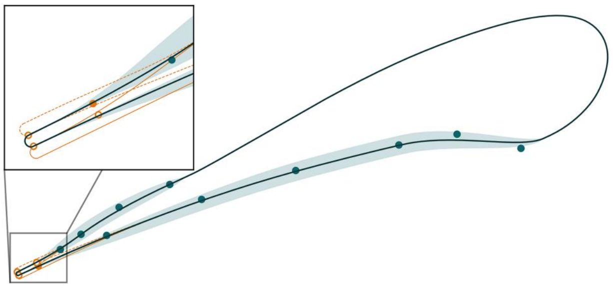

Fig. 9 Design space for the stator shape optimization. ● Moveable CPS along the blade profile; ● Moveable CP at the trailing edge; ○ CPS at the trailing edge that move rigidly with the moveable CP. (Color version online.)

enables the optimization routine to balance global exploration with local exploitation, enhancing the robustness of the search. The optimization framework used in this study is based on an in-house Python script, documented in Ref. [40], with minor modifications.

3.2.2 Geometry Parameterization. Figure 9 illustrates the base profile (solid black line) and the control points (CPs) that define the divergent section of the blade. The CPs associated with the convergent portion (not shown) remain fixed during optimization, as their minimal impact on cascade performance [41,42] does not justify the added computational cost of expanding the design space. Consequently, only 11 movable CPs, all located in the divergent section, are employed.

The same parameterization approach as the FORMA package [43] is applied. The blade is represented by a third-order B-spline curve, ensuring second-order continuity of the profile. The trailing edge is closed with an elliptical curve whose endpoints are tangent to the profile. Since the outlet blade angle is already correctly defined by the base profile, only one CP can move freely at the trailing edge, while the others adjust rigidly to maintain a constant outlet blade angle.

3.2.3 Objective Function and Constraint. The objective function to be minimized is the total loss coefficient (Y), defined as:

$$Y = \frac{P_{t,\mathrm{in}} - P_{t,\mathrm{out}}}{P_{t,\mathrm{in}} - P_{\mathrm{out}}} \tag{20}$$

where the outlet quantities are computed at the rotor inlet radial coordinate, to account for the losses within the blade passage and at the trailing edge.

A single constraint is imposed on the mass flowrate, which can differ up to ±1% from the value computed by the cycle optimization. This constraint is necessary because the choked nature of the stator forces the mass flowrate in the entire system and thus the power output.

3.2.4 Computational Fluid Dynamics Framework. As discussed in Sec. 3.2.1, the proposed designs are evaluated using CFD simulations. The selected solver is a steady, pressure-based homogeneous equilibrium model that solves the Favre-averaged Navier–Stokes equations, incorporating equilibrium thermodynamic properties.

In the employed framework, the original energy equation in ANSYS-Fluent®, expressed in terms of total enthalpy, is rewritten in an enthalpy-based form via a user-defined function. This allows us to replace the standard thermodynamic pair employed by ANSYS-Fluent® (P, T) - which is not independent in the two-phase region—with the independent pair (P, h). The interested reader can consult Romei et al. [44] for a more in-depth explanation of the model implementation.

The turbulence is modeled with the state-of-the-art k-ω-SST model with a resolved boundary layer (maximum y^+ lower than 5 and area-averaged y^+ below 2).

To speed up the computation, look-up tables are constructed before the simulations using the Span–Wagner model implemented in CoolProp [32]. A coupled scheme and least-squares cell-based discretization for the gradient are employed, along with second-order discretization for the pressure term and second-order upwind discretization for the remaining terms.

The domain is discretized with a quasi-three-dimensional mesh of only one blade, created with ANSYS-Turbogrid®, due to the constant profile shape along the spanwise direction, thus reducing the computational burden. Consequently, a symmetry boundary condition on both the hub and shroud is employed, while side boundaries are modeled as periodic. The other imposed conditions are no-slip and adiabatic wall on the blade, the total thermodynamic conditions at the inlet, and the static pressure at the outlet.

The base profile was simulated with four meshes of different sizes to assess the effect of the element number on the loss coefficient. The pitch-wise pressure trend reported in Fig. 10 shows that the three cases differ primarily in the shock proximity, i.e., at $\Delta\theta/\theta = 0.33$ and $\Delta\theta/\theta = 0.78$. As expected, the Y decreases with the increase of the element number because of a lower numerical diffusion, as shown in Table 5.

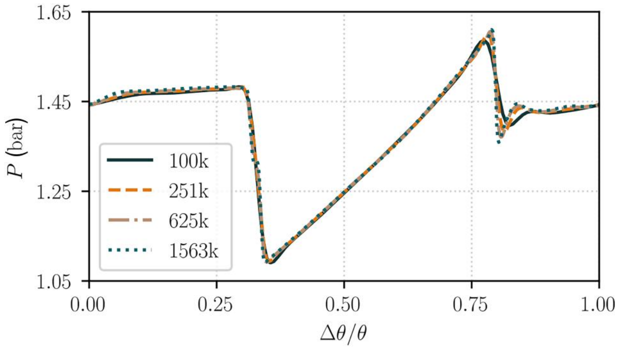

Fig. 10 Pitch-wise distribution of base stator pressure trend at the rotor inlet radius for different mesh sizes

Table 5 Loss coefficient and total computational time of the base case for different number of elements in the blade-to-blade plane

Number of elements	100 k	251 k	625 k	1563 k
Y (%)	14.28	14.26	13.54	13.25
t_{comp} (s)	464	1076	4241	10,521

Although these results suggest the use of the 625 k mesh, the required computational time, based on simulations performed with 20 processors (Intel(R) Xeon(R) Gold 6242R) on a cluster, makes this choice not acceptable for an optimization process that will involve approximately 240 CFD simulations. From the optimization point of view, the best choice is the 100 k mesh, which guarantees the lowest computational burden while keeping the actual profile classification made by the optimization routine. The optimum profile is resimulated with a 625 k element mesh to confirm this assumption. The Y computed with the 100 k, equal to 11.80%, is higher than the optimum Y computed with the 625 k mesh (values in Table 6) with a relative difference similar to the one between the 100 k and 625 k base profile meshes.

3.2.5 Base Versus Optimum Stator Design. To assess the effectiveness of the shape optimization, a comparison between the base and the optimum profile is presented in this section. Note that, while the optimization routine has been made with the 100 k mesh, all the reported results are computed with 625 k elements on the blade-to-blade plane.

The comparison of loss coefficient Y, reported in Table 6, proves that the optimization routine improved the profile performance, with a relative loss decrease of about 20%. Both profile mass flow rates are close to the design value of 1.62 kg/s, staying in the error band of ±1%. The optimum blade angle α and Mach number M are respectively 0.64 deg (0.86%) and 0.01 (0.55%) lower than their corresponding values computed by the mean-line, which are 74.60 deg and 1.82. The reasons behind these differences are explained in more depth in the later part of this Section.

Table 6 Integral quantities comparison between base and optimum blade computed with the 625 k Mesh

Case	Y (%)	$\dot{m}$ (kg/s)	M_{av}	α_{av} (deg)
Base	13.54	1.61	1.81	74.46
Optimum	11.28	1.63	1.81	73.96

M_{av} and α_{av} are mass-averaged quantities.

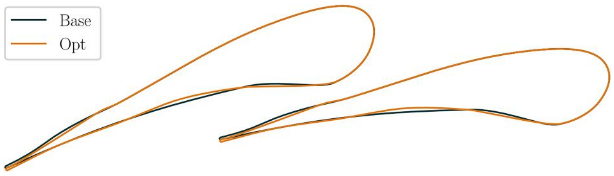

Fig. 11 Comparison between the base and the optimum blade profiles

The performance improvement is primarily the result of changes in the blade profile, as shown in Fig. 11. While the throat area and location remain similar—with only a slight increase in the former, as indicated by the higher $\dot{m}$ reported in Table 6 more significant changes are observed in the divergent portion of the blade profile.

To better understand the effects of the profile optimization, Fig. 12 presents the contours of M and the density gradient for both the base and optimum profiles. The most notable difference between the two profiles is the decrease in the intensity of the fish-tail shocks, marked as (i) and (ii) in the density gradient contour shown in Fig. 12. This reduction is achieved by increasing the outlet blade passage area, as seen in Fig. 11, which allows the flow to approach the adapted conditions. A further contribution to loss reduction comes from the intensity decrease of shock (iii). This shock is formed by a series of compression waves originating from the blade pressure side, which subsequently coalesce and are then reflected as a shock by the suction side. The intensity reduction of this shock is mainly due to the lower compression entailed, through the waves, by the optimized profile. This is accomplished by modifying the pressure side and translating the trailing edge.

In both the base and optimum profiles, a small shock originating from the suction side, identified as (iv), is present, with nearly the same intensity. Due to its low intensity and minimal contribution to the overall losses, the optimization primarily focuses on reducing the intensity of the other shocks, rather than eliminating shock (iv).

Finally, it is interesting to note that the discontinuity in the density gradient, located at the rotor inlet and caused by the combination of shocks (iii) and (i), is more pronounced in the optimum profile compared to the base profile. This counterintuitive observation results from a series of compression waves formed on the suction side, which combine with the aforementioned shocks. This also explains why the optimum profile shows a greater change in both M and α profiles at $\Delta\theta/\theta = 0.45$, see Fig. 13, compared to the base case.

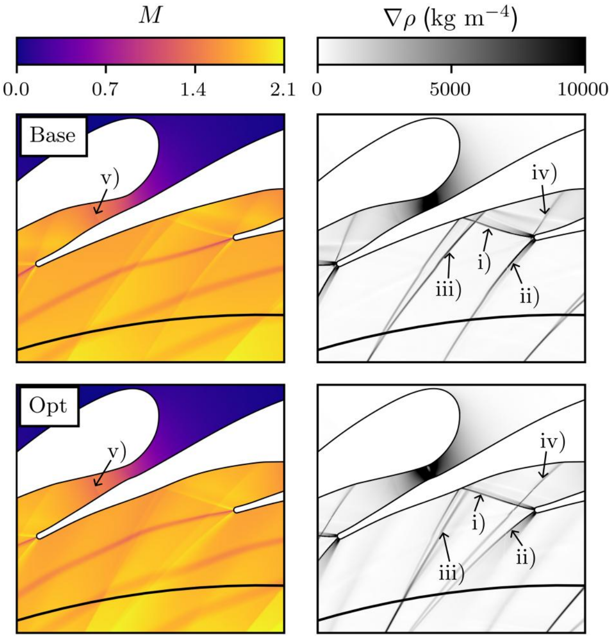

Fig. 12 Mach (left) and density gradient (right) contours of the base and optimum profiles. The black continuous line identify the rotor inlet radial coordinate.

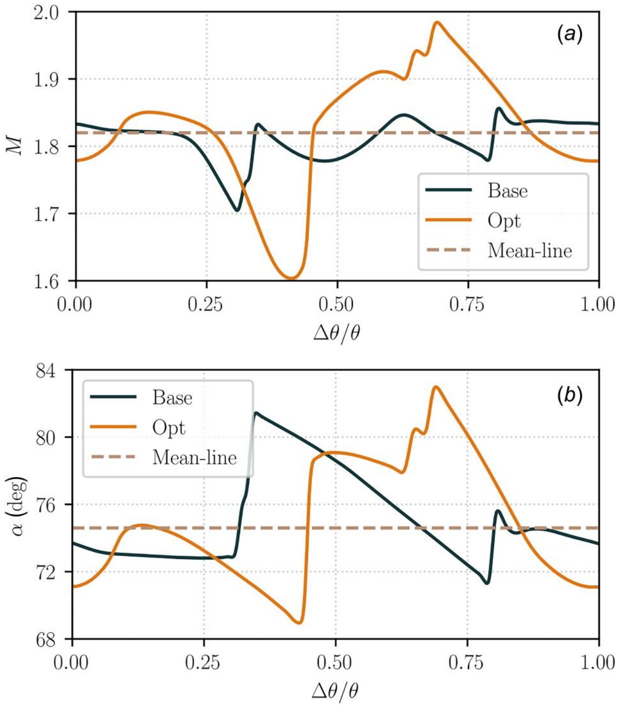

Fig. 13 Pitch-wise distribution of (*a*) Mach and (*b*) absolute flow angle at the rotor radial position for the base and optimum profiles

A barely measurable Mach discontinuity is observed at the vaporization end, marked as (v) in the Mach contours. Due to the vapor quality at the cascade inlet, the Mach nonmonotonicity associated with the phase change is not observed, except at the location of the vaporization end, as previously identified.

While the averaged values of M and α of the base and optimum profile reported in Table 6 are very similar, their pitch-wise trends differ significantly, as shown in Fig. 13. More precisely, the base profile trends present two fluctuations at $\Delta\theta/\theta = 0.33$ and $\Delta\theta/\theta = 0.78$ related to the two shocks that cross the rotor inlet radial coordinate, as observable in Fig. 12. About the optimum profile, it is visible the effect on the trends of the shock at $\Delta\theta/\theta = 0.45$, as noted before, explaining the lower average value of α. Additionally, the coalescence of shocks (ii) and (iv) is shifted at a lower radial coordinate, while the discontinuity observed at the rotor inlet is shifted at about $\Delta\theta/\theta = 0.70$.

Furthermore, the vapor quality contour of the optimum blade, shown in Fig. 14, indicates that complete vaporization occurs well before the outlet of the blade passage, as indicated by the location of the white curve. This confirms that the goal of confining the two-

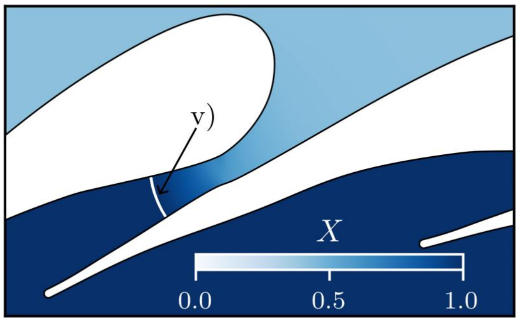

Fig. 14 Vapor quality contour of the optimum profile. The white line in the blade passage, identified with v), localized the vaporization end.

phase expansion within the stator is achieved. The vapor quality contour of the base profile is similar to that of the optimum profile, so it is not presented here for the sake of brevity.

In summary, the proposed shape optimization successfully improved stator performance while meeting the target mass flowrate and thermodynamic conditions at the rotor inlet.

3.3 Complete Turbine Computational Fluid Dynamics Simulation Results. In this section, a comparison is presented between the efficiency predicted by the mean-line code and the efficiency computed from the complete turbine simulation results, alongside a comparison of the loss breakdown. The simulated turbine consists of all the components shown in Fig. 8. The stator geometry is the optimized one, while the rotor is designed using the mean-line results, without any optimization, due to the more consolidated design practices for this cascade.

Due to the high blade deflection in the rotor (approximately 108 deg), an incidence angle of around 28 deg is accepted to achieve a feasible rotor blade geometry. The simulated diffuser geometry also differs slightly from the sketch in Fig. 8. Specifically, the sudden area change associated with the ogive is replaced by a gradual area increase, maintaining the same semi-angle opening of the diffuser tip. This modification allows to avoid flow detachment, which would complicate the simulation convergence.

The CFD framework used is similar to the one described in Sec. 3.2.4, with minor adjustments. A mixing plane interface has been implemented to connect the stationary and rotating domains, enabling mass-averaged quantities to pass from the stator to the rotor. As a result, only one blade per cascade is simulated, exploiting periodic boundary conditions. About the meshes, the stator is discretized with 100 k elements on the blade-to-blade plane, with a total number of elements of 4400 k in the domain, while the rotor is discretized with 150 k elements on the blade-to-blade plane. A tip clearance of 0.5 mm is also included in the rotor domain and is discretized with 26 elements along the spanwise direction. The total number of elements in the rotor domain, considering the rotor, the tip clearance, and the diffuser, which is discretized with a coarser mesh to reduce the computational burden, is 7788 k. In all domains, the boundary layer is completely resolved, with a maximum y^+ lower than 5 and an area-averaged y^+ below 2.

The comparison between the two cases shows a reduction in the total-to-static efficiency from 89.6% (computed by the mean-line code) to 87.4% for the CFD simulation. This difference is in line with the maximum overprediction of 3% observed during the mean-line validation process [27].

The loss breakdown, shown in Fig. 15, reveals a generally good agreement between the mean-line and CFD results, except for the stator. This discrepancy may be due to the additional losses introduced by the fish-tail shocks, connected to the not-adapted flow at the stator outlet, which are not taken into account by the employed mean-line code. Regarding other contributions, the higher kinetic energy at the turbine outlet (denoted as KE in Fig. 15) is related to the different diffuser geometry, while the diffuser loss contributions are similar in both cases. This suggests that the losses predicted by the model of Agromayor et al. [30] are very similar to those computed from the CFD when the skin friction coefficient proposed in the referenced paper is used. The higher losses in the rotor are primarily due to flow detachment on the rotor suction side, which is visible in the Mach contour at midspan, shown in Fig. 16. This is mainly caused by the high flow deflection, and its intensity increases with the span, as seen in the dissipation field in the same figure.

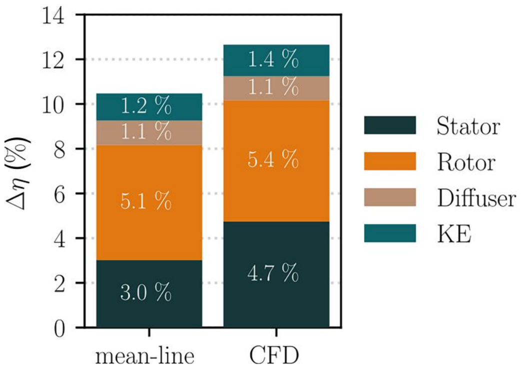

Fig. 15 Loss breakdown comparison between mean-line and CFD. The CFD results have been post-processed to obtain the mixed-out state with the procedure presented in Ref. [44].

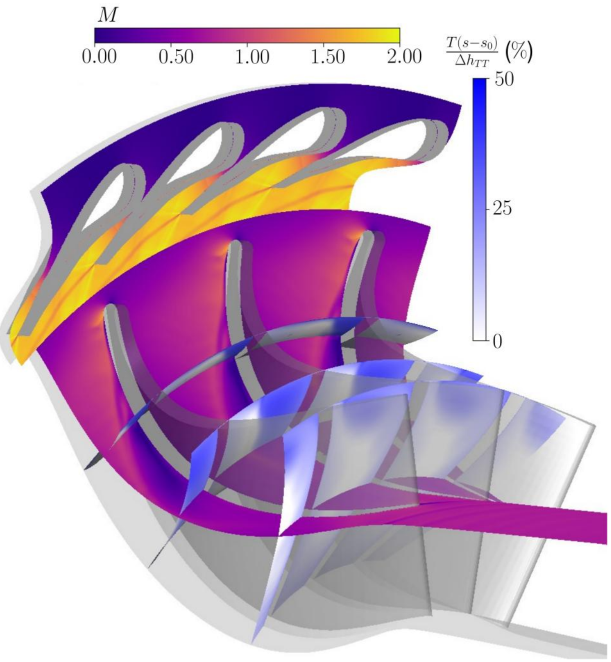

Fig. 16 Mach contour at midspan and dissipation field at different streamwise coordinates of the simulated total turbine

While the majority of the flow within the rotor remains subsonic, a small region of slightly supersonic flow exists on the suction side right after the leading edge, likely due to the accepted incidence angle. Although flow detachment and supersonic flow are undesirable, their minimal impact on turbine efficiency makes them acceptable for the nonoptimized geometry presented here.

In conclusion, this section demonstrates that it is possible to design a two-phase radial inflow turbine with an efficiency greater than 85% assumed during the cycle optimization.

4 Conclusion

This study addressed the challenges of designing MW-scale PE-ORC systems for industrial waste heat recovery. The first part focused on developing a cycle model to identify optimal working fluids and operating conditions, tested through two case studies representing different heat source temperatures. In the high-temperature case study, Cyclopentane resulted in the optimal fluid with a dry-expansion cycle without a recuperator, with a pressure ratio of 62. In the low-temperature case, Novec649 demonstrated the highest power output with a turbine inlet vapor quality of 0.42 and a pressure ratio of 17. The low-temperature case was selected for the second part of the study, which focused on the preliminary design of a radial inflow turbine for PE cycles with wet-to-dry expansion. The design demonstrated that confining two-phase expansion within the stator is feasible using a single-stage radial inflow turbine.

The preliminary geometry was defined using an in-house mean-line model and refined through CFD simulations. Efforts were focused on the stator, featuring a convergent-divergent geometry designed to minimize losses and ensure complete vaporization at the outlet. The presented optimization process enhanced the efficiency by reducing shock intensity.

The results showed that the turbine overall efficiency remains competitive, with a total-to-static efficiency of about 87.4% (thus above 85%), proving the feasibility of designing turbines for PE-ORCs at an industrial scale. However, further validation of CFD models for two-phase flows, currently not possible due to the lack of experimental data, is required.

This work provides a strong foundation for future developments and the broader implementation of two-phase turbines in the framework of PE-ORCs, promoting the sustainable recovery of waste thermal energy.

Acknowledgment

We acknowledge financial support under the National Recovery and Resilience Plan (NRRP), Mission 4, Component 2, Investment 1.1, Call for tender No. 1049 published on 14.9.2022 by the Italian Ministry of University and Research (MUR).

Funding Data

- European Union—NextGenerationEU—Project Title POWHER: Partial evaporation ORC systems for industrial Waste Heat Recovery (Award ID: CUP D53D23018390001—Grant Assignment Decree No. 1385; Funder ID: 10.13039/501100003407).

Data Availability Statement

The datasets generated and supporting the findings of this article are obtainable from the corresponding author upon reasonable request.

Nomenclature

CFD = computational fluid dynamics
CP = control point
GWP = global warming potential
h = specific enthalpy (kJ/kg)
HEM = homogeneous equilibrium model
HT = high temperature
Ja = Jacob number
LT = low temperature
M = Mach number
$\dot{m}$ = mass flow rate (kg/s)
MoC = method of characteristics
ODP = ozone depletion potential
ORC = organic Rankine cycle
P = pressure (MPa)
PE = partial evaporation
P_r = reduced pressure
P_t = total pressure (bar)
$\dot{Q}$ = thermal power (kW)
r = radius (m)
s = specific entropy (kJ/kg/K)
T = temperature (K)
TRL = technology readiness level
t_{comp} = CFD computational time (s)
$\dot{V}$ = volumetric flow rate (m^3/s)
VR = volume expansion ratio
$\dot{W}$ = power (kW)
WHR = waste heat recovery
X = vapor quality
Y = pressure loss coefficient
y^+ = Y plus

Greek Symbols

α = absolute flow angle (deg)
β = pressure ratio
β_{TS} = total-to-static pressure ratio
$\frac{\Delta\theta}{\theta}$ = non-dimensional pitchwise coordinate
ε = heat transfer effectiveness
η = efficiency
ρ = density (kg/m^3)
$\nabla\rho$ = density gradient (kg/m^4)
σ = molecular complexity (kJ/kg/K^2)

Subscripts

av = mass-averaged quantity
C, in/out = cold sink in/out
crit = critical
em = electromechanical
ev = evaporator
H, in/out = hot source in/out
in = control volume inlet
is = isentropic
k = condensation
l = liquid
ORC = Cycle
out = control volume outlet
p = pump
pp = pinch point
rec = recuperator
rot, out, h = rotor outlet hub
rot, out, sh = rotor outlet shroud
sc = subcooling
sh = superheating
tot = total
turb = turbine
v = vapor
vap = vaporization

References

[1] Agathokleous, R., Bianchi, G., Panayiotou, G., Aresti, L., Argyrou, M. C., Georgiou, G. S., Tassou, S. A., et al., 2019, “Waste Heat Recovery in the EU Industry and Proposed New Technologies,” Energy Proc., **161**, pp. 489–496.

[2] Astolfi, M., Baresi, M., Van Biert, L., van Buijtenen, J., Casella, F., Colonna, P., Karellas, S., Lemort, V., Öhman, H., Ribarov, L., Sánchez, D., White, M., and Wieland, C., 2025, “Thermal Energy Harvesting: The Path to Tapping into a Large CO$_2$-free European Power Source,” Delft, The Netherlands.

[3] Macchi, E., and Marco, A., 2017, *Organic Rankine Cycle (ORC) Power Systems: Technologies and Applications*, Woodhead Publishing, Duxford.

[4] Smith, I. K., 1993, “Development of the Trilateral Flash Cycle System: Part 1: Fundamental Considerations,” Proc. Inst. Mech. Eng., Part A, **207**(3), pp. 179–194.

[5] DiPippo, R., 2007, “Ideal Thermal Efficiency for Geothermal Binary Plants,” Geothermics, **36**(3), pp. 276–285.

[6] Fischer, J., 2011, “Comparison of Trilateral Cycles and Organic Rankine Cycles,” Energy, **36**(10), pp. 6208–6219.

[7] Smith, I. K., Stošič, N., and Aldis, C. A., 1996, “Development of the Trilateral Flash Cycle System: Part 3: The Design of High-Efficiency Two-Phase Screw Expanders,” Proc. Inst. Mech. Eng., Part A, **210**(1), pp. 75–93.

[8] Bianchi, G., McGinty, R., Oliver, D., Brightman, D., Zaher, O., Tassou, S. A., Miller, J., and Jouhara, H., 2017, “Development and Analysis of a Packaged Trilateral Flash Cycle System for Low Grade Heat to Power Conversion Applications,” Therm. Sci. Eng., **4**, pp. 113–121.

[9] Ottaviano, S., Poletto, C., Ancona, M. A., and Melino, F., 2022, “Experimental Investigation on micro-ORC System Operating With Partial Evaporation and Two-Phase Expansion,” Energy Convers. Manage., **274**, p. 116415.

[10] Read, M. G., Smith, I. K., and Stošič, N., 2017, “Optimisation of Power Generation Cycles Using Saturated Liquid Expansion to Maximise Heat Recovery,” Proc. Inst. Mech. Eng., Part E, **231**(1), pp. 57–69.

[11] Lai, N. A., and Fischer, J., 2012, “Efficiencies of Power Flash Cycles,” Energy, **44**(1), pp. 1017–1027.

[12] Elliott David, G., 1982, “Tests of a Two-Stage, Axial-Flow, Two-Phase Turbine,” Jet Propulsion Laboratory (JPL), California Institute of Technology (CalTech), Pasadena, CA, Report No. DOE/ER/10614-2.

[13] White, M. T., 2021, “Cycle and Turbine Optimization for an ORC Operating With Two-Phase Expansion,” App. Therm. Eng., **192**, p. 116852.

[14] White, M. T., 2022, “Investigating the Wet-to-Dry Expansion of Organic Fluids for Power Generation.,” Int. J. Heat Mass Transfer, **192**, p. 122921.

[15] Zhu, J., and Elbel, S., 2019, “Measurement of Static Pressure Profiles of Vortex Flashing R134a Flow Expanded Through Convergent–Divergent Nozzles,” Int. J. Refrig., **108**, pp. 258–270.

[16] Zhu, J., and Elbel, S., 2020, “CFD Simulation of Vortex Flashing R134a Flow Expanded Through Convergent-Divergent Nozzles,” Int. J. Refrig., **112**, pp. 56–68.

[17] Tammone, C., Romei, A., Persico, G., and Haglind, F., 2022, “Non-Equilibrium Phenomena in Two-Phase Flashing Flows of Organic Fluids,” Proceedings of the

4th International Seminar on Non-Ideal Compressible Fluid Dynamics, Vol. 29, Springer, Cham.

[18] CoolProp, 2023, “High-Level Interface - CoolProp 6.4.3 Documentation,” CoolProp Developers, Belgium, accessed July 3, 2023, http://www.coolprop.org/coolprop/HighLevelAPI.html

[19] Scagnolatto, G., Cabezas-Gómez, L., and Bigonha Tibiriçá, C., 2021, “Analytical Model for Thermal Efficiency of Organic Rankine Cycles, Considering Superheating, Heat Recovery, Pump and Expander Efficiencies,” Energy Convers. Manage., **246**, p. 114628.

[20] Bamorovat Abadi, G., and Kim, K. C., 2017, “Investigation of Organic Rankine Cycles With Zeotropic Mixtures as a Working Fluid,” Renewable Sustainable Energy Rev., **73**, pp. 1000–1013.

[21] Blank, J., and Deb, K., 2020, “Pymoo: Multi-Objective Optimization in Python,” IEEE Access, **8**, pp. 89497–89509.

[22] Exergy SpA, 2009, “Cementirossi,” accessed Mar. 4, 2024, https://www.exergy-orc.com/casi853studio/cementirossi/studio/cementirossi/

[23] Turboden SpA, 1980, “HSY,” accessed Mar. 4, 2024, https://www.turboden.com/

[24] Exergy SpA, 2011, “PTT LNG Rayong,” accessed Mar. 4, 2024, https://www.exergy-orc.com/855casi-studio/ptt-lng-rayong/

[25] Zuccato Energia, 2006, “Emilia Romagna 01-2021,” Verona, Italy, accessed Mar. 4, 2024, https://zuccatoenergia.it/en/references/emilia-romagna-01/

[26] Romei, A., Giostri, A., and Spinelli, A., 2024, “Feasibility of Solar-Driven Trilateral-Like Organic Rankine Cycle With Radial-Inflow Turboexpander,” Appl. Therm. Eng., **257**, p. 124239.

[27] Manfredi, M., Alberio, M., Astolfi, M., and Spinelli, A., 2021, “A Reduced-Order Model for the Preliminary Design of Small-Scale Radial Inflow Turbines,” ASME Paper No. GT2021-59444.

[28] Glassman, A. J., 1976, “Computer Program for Design Analysis of Radial-Inflow Turbines,” NASA Lewis Research Center Cleveland, OH, Report No. NASA-TN-D-8164.

[29] Chisholm, D., 1967, “A Theoretical Basis for the Lockhart-Martinelli Correlation for Two-Phase Flow,” Int. J. Heat Mass Transfer, **10**(12), pp. 1767–1778.

[30] Agromayor, R., Muller, B., and Nord, L. O., 2019, “One-Dimensional Annular Diffuser Model for Preliminary Turbomachinery Design,” Int. J. Turbomach. Propul. Power, **4**(3), p. 31.

[31] Liao, Y., and Lucas, D., 2021, “A Review on Numerical Modelling of Flashing Flow With Application to Nuclear Safety Analysis,” Appl. Therm. Eng., **182**, p. 116002.

[32] Bell, I. H., Wronski, J., Quoilin, S., and Lemort, V., 2014, “Pure and Pseudo-Pure Fluid Thermophysical Property Evaluation and the Open-Source Thermophysical Property Library CoolProp,” Ind. Eng. Chem. Res., **53**(6), pp. 2498–2508.

[33] Lemmon, E. W., Bell, I. H., Huber, M. L., and McLinden, M. O., 2018, *NIST Standard Reference Database 23: Reference Fluid Thermodynamic and Transport Properties-REFPROP, Version 10.0*, Standard Reference Data Program, Gaithersburg, MD, pp. 45–46.

[34] Antonio, P., and Lozza, G., “Design Criteria and Efficiency Prediction for Radial Inflow Turbines,” ASME Paper No. 87-GT-231.

[35] Zucrow, M. J., and Hoffman, J. D., 1977, *Gas Dynamics, Volume 2*, Krieger Publishing Company, Malabar, FL.

[36] Zocca, M., Gajoni, P., and Guardone, A., 2023, “NIMOC: A Design and Analysis Tool for Supersonic Nozzles Under Non-Ideal Compressible Flow Conditions,” J. Comput. Appl. Math., **429**, p. 115210.

[37] Rinaldi, E., Pecnik, R., and Colonna, P., 2016, “Unsteady Operation of a Highly Supersonic Organic Rankine Cycle Turbine,” ASME J. Turbomach., **138**(12), p. 121010.

[38] Forrester, A. I. J., Keane, A. J., and Bressloff, N. W., 2006, “Design and Analysis of ‘Noisy’ Computer Experiments,” AIAA J., **44**(10), pp. 2331–2339.

[39] Jones, D. R., Schonlau, M., and Welch, W. J., 1998, “Efficient Global Optimization of Expensive Black-Box Functions,” J. Global Optim., **13**(4), pp. 455–492.

[40] Kamali, K., Gaetani, P., Persico, G., and Romei, A., 2024, “CFD-Based Shape Optimization of Flashing Converging-Diverging Nozzles in Pelton Turbines for Domestic Carbon Dioxide Heat Pumps Including Off-Design Conditions,” Appl. Therm. Eng., **257**, p. 124321.

[41] Pini, M., Persico, G., Pasquale, D., and Rebay, S., 2015, “Adjoint Method for Shape Optimization in Real-Gas Flow Applications,” ASME J. Eng. Gas Turbine Power, **137**(3), p. 032604.

[42] Romei, A., and Persico, G., 2018, “Novel Shape Parametrization Technique Applied to the Optimization of a Supersonic ORC Turbine Cascade,” ASME Paper No. GT2018-76732.

[43] Persico, G., Rodriguez-Fernandez, P., and Romei, A., 2019, “High-Fidelity Shape Optimization of Non-Conventional Turbomachinery by Surrogate Evolutionary Strategies,” ASME J. Turbomach., **141**(8), p. 081010.

[44] Romei, A., Gaetani, P., and Persico, G., 2022, “Computational Fluid-Dynamic Investigation of a Centrifugal Compressor With Inlet Guide Vanes for Supercritical Carbon Dioxide Power Systems,” Energy, **255**, p. 124469.